Inferring Critical Slip-Weakening Distance from Near-Fault Accelerogram of the 2014 M_w 6.2 Ludian Earthquake

Xiang Chen[1], Hongfeng Yang[*1,2], and Mingpei Jin[3]

Abstract

To better assess potential earthquake hazards requires a better understanding of fault friction and rupture dynamics. Critical slip-weakening distance (D_c) as one of the key friction parameters, however, is hard to determine on natural faults. For strike-slip earthquakes, we may directly estimate the D_c from D_c''—the double near-fault ground displacement at the time of the peak velocity (Fukuyama and Mikumo, 2007). Yet near-fault observations are very few, and, thus, there were only limited earthquakes with such D_c'' estimation. In 2014, an M_w 6.2 strike-slip event—the Ludian earthquake—occurred in southwest China. The strong-motion station (LLT) that is ~0.45 km from the fault recorded the earthquake and enabled us to estimate D_c'' from the accelerograms. We inspect the polarity of the accelerometers and compare the integrated velocities with waveforms of nearby broadband stations. We also analyze the particle motion at the LLT station and retrieve the earthquake initiation at the intersection of the conjugated faults. We then apply the baseline correction to the seismograms, recover the ground velocities and displacements, and obtain the value of $D_c'' = 0.1$ m at the station. The recovered final displacements are compared with the predicted ground displacements of a finite-fault model. The discrepancy of fault-parallel displacements might imply limited underestimation of D_c'', and the estimated upper limit is 0.3 m. Comparison between the D_c'' and final slip on the fault patch follows the scaling of previous larger earthquakes. Analysis of the near-fault accelerometer data enhances our understanding on the earthquake source of the Ludian earthquake. This case extends the lower magnitude boundary of the D_c'' values obtained from natural faults and opens a window into the friction property in the seismically active region.

Introduction

Fault-weakening process is of great significance for both understanding the earthquake source and seismic hazard mitigation. One of the governing laws—linear slip-weakening law (Ida, 1972; Andrews, 1976a,b)—has been widely used to depict the weakening process, in which the shear stress linearly declines from peak strength (τ_s) to the dynamic stress level (τ_d) during a portion of accumulated slip (D_c). As an important fault weakening parameter, D_c could affect the earthquake energy budget and influence the final earthquake slip and extent. Because of the strong trade-off between D_c and the strength excess (Guatteri and Spudich, 2000; Goto and Sawada, 2010), the parameter D_c is of complexity to constrain on natural faults from observational seismic data and may require the combination of multiple observations (Weng and Yang, 2018; Yao and Yang, 2020).

For strike-slip earthquakes with near-fault observations, a direct method was arisen to estimate the critical slip-weakening distance D_c (Fig. 1, Fukuyama *et al.*, 2003; Mikumo *et al.*, 2003; Fukuyama and Mikumo, 2007). D_c by definition refers to the slip amount at stress breakdown time (Fig. 1b); whereas according to the proximity of time moments of stress breakdown and peak slip rate, D_c could be approximated by the slip amount at the latter, denoted as D_c' (Fukuyama *et al.*, 2003; Mikumo *et al.*, 2003). For an off-fault station in the strike-slip fault (Fig. 1c), assuming the symmetric displacement distribution across the fault, twice of the fault-parallel displacement at the time of peak velocity (D_c'') could be regarded as an approximation of
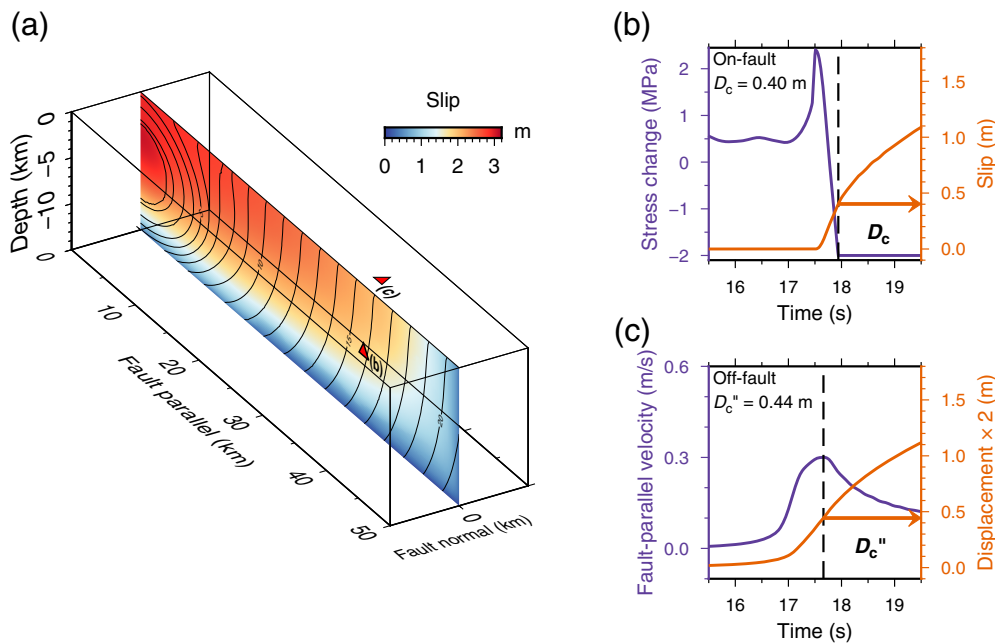
Figure 1. Illustration of the D_c'' method using a dynamic rupture model. (a) A 3D dynamic rupture model showing slip distribution on a vertical planar strike-slip fault. Curves on the fault are isochrones of the rupture fronts. Red triangles indicate the locations of the grids in subfigures (b) and (c), respectively. (b) Time history of stress change (purple curve), slip development (orange curve), and the definition of D_c for the grid on the fault shown in (a). (c) Time history of the fault-parallel ground velocity (purple curve), ground displacement evolution (orange curve), and the definition of D_c'' for the off-fault grid on the ground shown in (a). The color version of this figure is available only in the electronic edition.

D_c (Fukuyama and Mikumo, 2007). The method provides a direct and simple estimation of D_c in strike-slip earthquakes with near-fault observations and may likely be used more often, given the increasing number of dense near-fault arrays with three-component sensors (e.g., Jiang *et al.,* 2020; Yang *et al.,* 2021).

The method mentioned earlier has been investigated through numerical simulation studies (Cruz-Atienza *et al.,* 2009; Cruz-Atienza and Olsen, 2010; Chen and Yang, 2020). Although the deviation of the calculated D_c'' from the true D_c on the fault could be affected by various factors related to the ground motion, for example, off-fault distance, free-surface effect, rupture speed, seismogenic fault width, and low-velocity fault zone, the parameter of D_c'' could provide a first-order estimation of the frictional property D_c on the fault (Chen and Yang, 2020). Besides, the distance of the station from the seismogenic fault needs to be short enough to resolve the weakening information (Cruz-Atienza *et al.,* 2009). When the rupture speed reaches supershear velocity, the resolution distance from fault could increase to over 10 km (Cruz-Atienza and Olsen, 2010), but additional correction is required to get a reasonable estimation. In reality, it is rare to have near-field instruments within several hundred to thousand meters from the ruptured fault, which might be the main factor that

limits the application of this method. So far, there have been five earthquakes with near-fault instruments to compute the D_c'' values (Fig. 2 and Table 1), of which the off-fault distances of the stations are within 3 km (Fukuyama and Mikumo, 2007; Cruz-Atienza and Olsen, 2010; Fukuyama and Suzuki, 2016; Kaneko *et al.,* 2017). The near-fault observation is essential for the application of the method, and obtaining more D_c'' values would help to understand the frictional properties of different fault systems.

In this study, utilizing the near-fault accelerograms of the 2014 M_w 6.2 Ludian earthquake, we apply the D_c'' method to the accelerometer data after instrument inspection, source process validation, and careful data processing. The D_c'' value provides an estimation value of the critical slip-weakening distance on the seismogenic fault of the Ludian earthquake, of which the large shallow slip causes severe hazards to the local residents and requires comprehensive research on the earthquake source.

Ludian Earthquake and Tectonic Settings

In 2014, an M_w 6.2 strike-slip earthquake occurred in Ludian county, Yunnan province. The earthquake is located on the southeast edge of the Tibet plateau, which is tectonically complex and seismically active (Fig. 3a). The Ludian earthquake produced strong ground motion and induced secondary disasters, which caused 617 fatalities and economic loss of over 19.8 billion CNY (according to a Chinese report from Yunnan Earthquake Prevention and Disaster Reduction website). The large near-ground slip asperity is one of the factors leading to the severe ground damage (Yang and Yao, 2021) and has been constrained by multiple studies; for example, kinematic rupture inversion studies resolve large slip patch in the shallow 0–10 km depth (Liu *et al.,* 2014; Zhang, Xu, *et al.,* 2014; Niu *et al.,* 2020); the Ludian earthquake is reported to rupture the ground surface according to the observations of field surveys (Xu *et al.,* 2015).

The seismogenic fault of the Ludian earthquake was unmapped before the earthquake occurrence. Determination
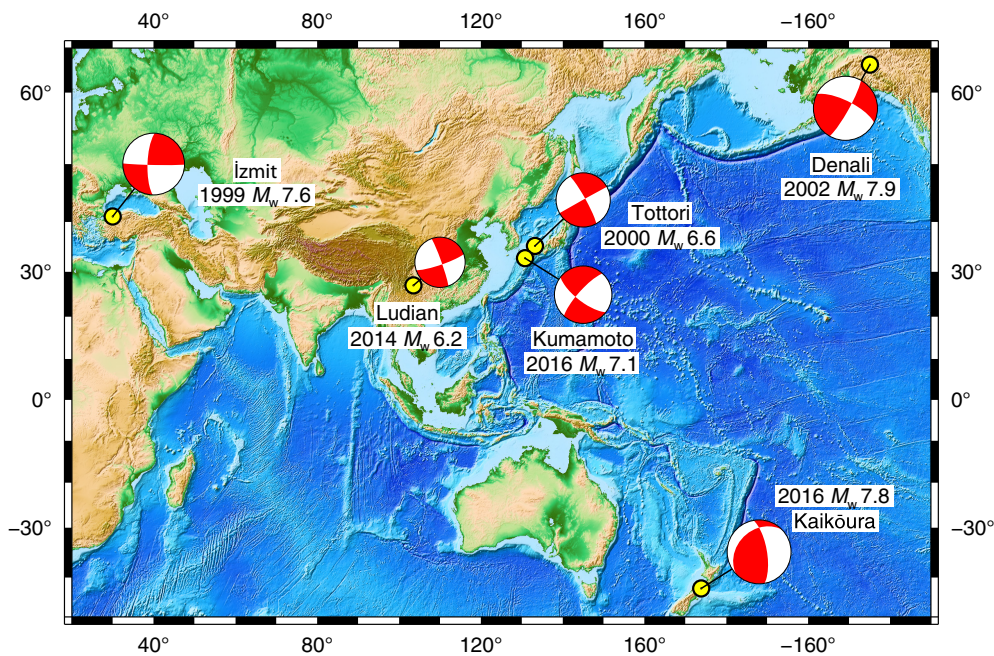
Figure 2. Distribution of the current application cases of the D_c'' method in natural earthquakes (Fukuyama and Mikumo, 2007; Cruz-Atienza and Olsen, 2010; Fukuyama and Suzuki, 2016; Kaneko *et al.*, 2017). The 2014 Ludian earthquake is the focus of this study. Information on focal mechanisms and earthquake locations is from the Global Centroid Moment Tensor (Global CMT) catalog (see Data and Resources). The color version of this figure is available only in the electronic edition.
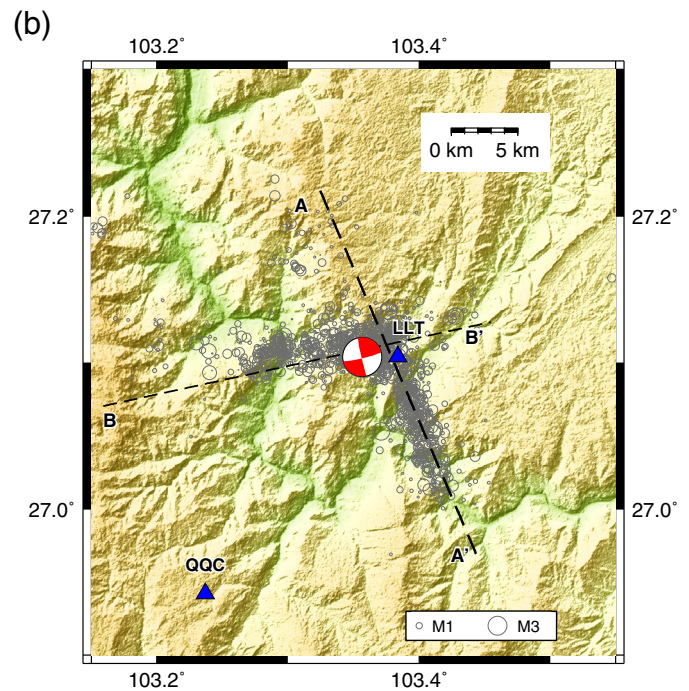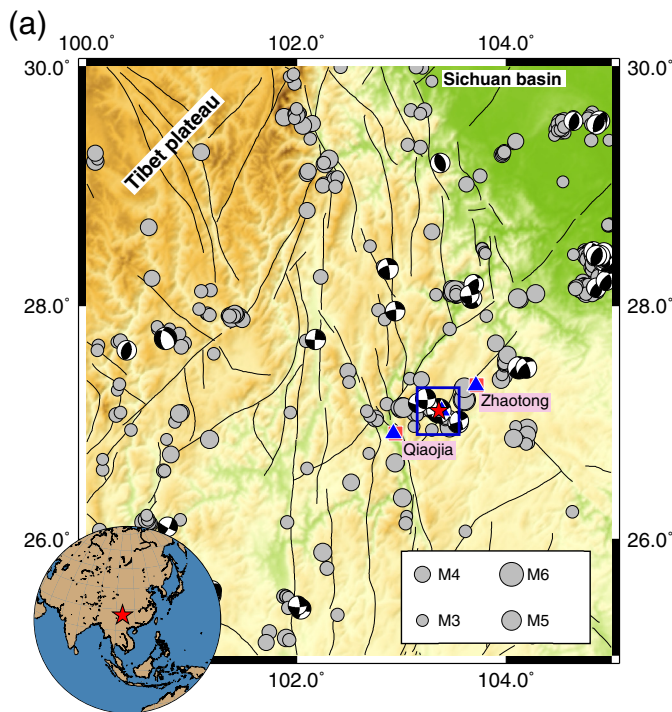
Ludian earthquake involved a conjugate fault system, as revealed by the aftershock distribution shown in Figure 3b (Cheng *et al.*, 2015), which brings in uncertainties about the rupture process of the Ludian earthquake. According to the aftershock distribution, two branches of the conjugate faults roughly extend on northwest–southeast and northeast–southwest direction (Fig. 3b). The northwest–southeast-trending branch is named Baogunao–Xiaohe fault in previous literatures, whereas another northeast–southwest-striking branch belongs to Zhaotong–Ludian fault.

To figure out the primary ruptured fault is essential for understanding the rupture process and for the acceleration data analysis. It is generally accepted that the northwest–southeast-trending fault is the primary seismogenic fault by multiple studies. As revealed by the finite-fault slip inversion, most of the coseismic slip is dominantly contributed by the northwest–southeast-striking fault (Liu *et al.*, 2014; Zhang, Xu, *et al.*, 2014; Luo *et al.*, 2018; Niu *et al.*, 2020), and the

of the fault plane is obtained from various observations, such as the aftershock distribution (Fang *et al.*, 2014; Wang *et al.*, 2014; Zhang, Lei, *et al.*, 2014; Cheng *et al.*, 2015) and field investigation (Li *et al.*, 2015; Xu *et al.*, 2015). The complexity is that the

TABLE 1
Global Application of the D_c'' Method (Modified after Chen and Yang, 2020)

Earthquake Information	Magnitude	D_c'' (m)	Station Off-Fault Distance (km)	Slip on the Corresponding Fault Segment (m)	D_c''/Total Slip	References
1999 İzmit	M_W 7.6	1.7*	2.8	4–5	~0.38	Cruz-Atienza and Olsen (2010)
2000 Tottori	M_W 6.6	0.3	0.1	1	0.3	Mikumo *et al.* (2003), Fukuyama and Mikumo (2007)
2002 Denali	M_W 7.9	2.5	~3	6.5	0.38	Fukuyama and Mikumo (2007)
		1.5*			0.23	Cruz-Atienza and Olsen (2010)
2016 Kumamoto	M_W 7.1	1	0.5	~2.3	0.43	Fukuyama and Suzuki (2016)
2016 Kaikōura	M_W 7.8	4.9	2.7	14	0.35	Kaneko *et al.* (2017)
2014 Ludian	M_W 6.2	0.1	0.45	0.3	0.33	This study

*The D_c'' values are obtained with the Mach-wave asymptotic correction and near-field adjustment, and, considering the free-surface amplification, a factor of 2 is divided compared to the definition of D_c'' in Fukuyama and Mikumo (2007).

Figure 3. (a) Seismotectonic setting of the 2014 Ludian earthquake and the seismicity in the surrounding region. Mainshock of the 2014 Ludian earthquake is shown as the red stars. Gray solid circles mark the M > 3 earthquakes in the region since 2009. The earthquake catalog is obtained from National Earthquake Data Center (see Data and Resources). Focal mechanism plots show the available earthquake focal mechanisms from the Global CMT catalog. The overlapping blue triangles and pink squares are the adjacent accelerometers and broadband stations in Qiaojia and Zhaotong, respectively. Inset: Location of the mainshock (red star). (b) Zoom-in map of the near-fault region of the 2014 Ludian earthquake shown in blue rectangular in (a). Gray hollow circles show the relocated aftershocks of the 2014 Ludian earthquake (Cheng et al., 2015). Two dashed lines indicate the conjugated fault planes (Niu et al., 2020), in which the thicker dashed line labeled AA′ is the primary fault that contributed most of the coseismic slip (Niu et al., 2020). Blue triangles mark the accelerometer locations. Red focal mechanism plot shows the focal mechanism of the 2014 Ludian mainshock from Liu et al. (2014). The color version of this figure is available only in the electronic edition.

single-plane inversion result shows that the northwest–southeast-trending faulting makes better waveform fitting, especially in the stations located in the strike direction (Liu et al., 2014). The rupture directivity analyses from the difference of the centroid location and the hypocenter (He et al., 2015) and apparent rupture duration inversion (Zhao et al., 2014) suggest a rupture direction from northwest direction toward southeast direction. Besides, the elongated isoseismal distribution in the northwest–southeast direction on the ShakeMap (Cheng et al., 2015) and the early aftershock trending within 1–2 hr after the mainshock (Fang et al., 2014; Liu et al., 2014) also imply the northwest–southeast-striking fault as the primary seismogenic fault of the Ludian mainshock.

Instrument and Data Inspection
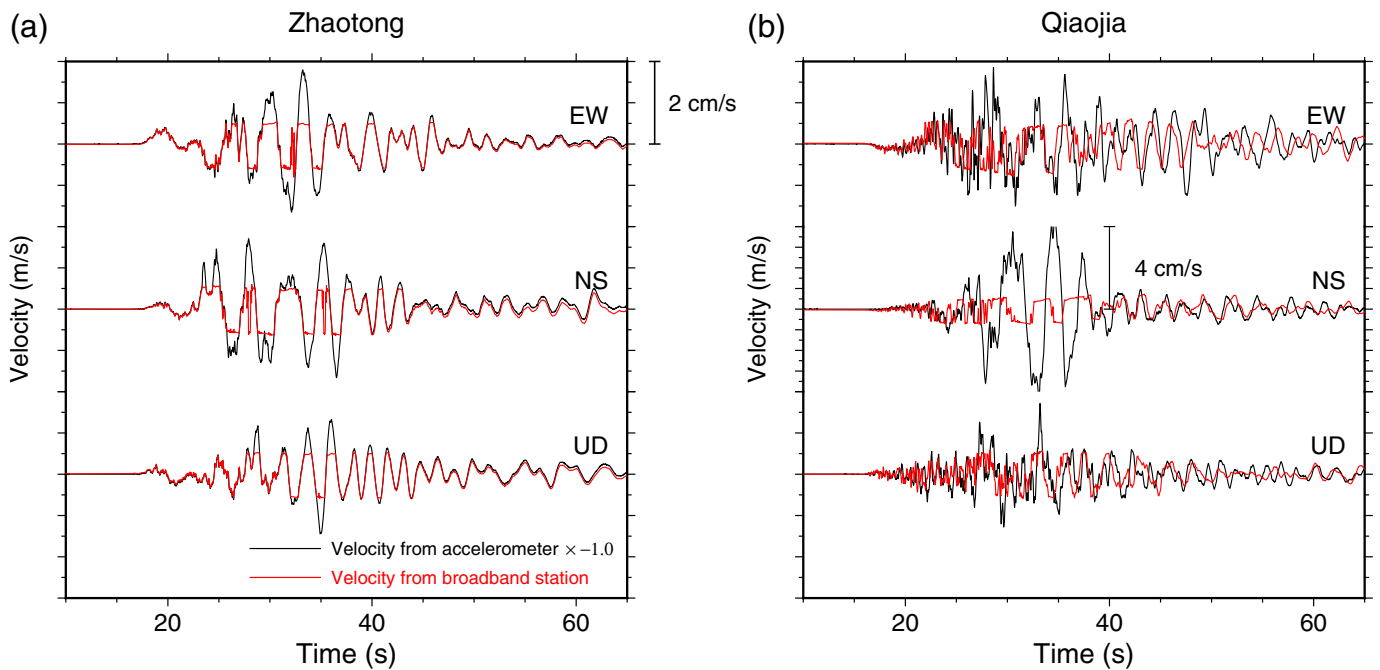### Acceleration data and method

The application of D_c'' estimation relies on the availability of near-fault coseismic observations. During the Ludian earthquake, a strong-motion station, the LLT station is located extremely close to the seismogenic fault of the Ludian earthquake (Fig. 3b) and captures the near-source strong-motion record of the earthquake, which provides us the chance to apply the D_c'' calculation to the Ludian earthquake and take a close look at the earthquake process.

The LLT station is located at 103.384° E, 27.104° N, which is ~0.45 km off the northwest–southeast-trending seismogenic fault plane inferred by Niu et al. (2020) and ~3 km from the relocated mainshock epicenter (Cheng et al., 2015). It recorded a peak ground acceleration of 949 Gal in the east–west component during the M_w 6.2 Ludian mainshock. The LLT station is equipped with a Kinemetrics ETNA

accelerograph, and the inner sensor is force-balance type SLJ-100 with a scale range of ±2g. This station is a part of the accelerometer network operated by the China Strong Motion Networks Center (see Data and Resources), of which more than 10 instruments are located within 100 km from the 2014 Ludian earthquake, and most of them are equipped with the same type instruments.

We first briefly describe how to estimate critical slip-weakening distance D_c from near-fault observations. In Figure 1a, we show a synthetic strike-slip earthquake rupture. For a slip patch on the fault, the critical slip-weakening distance D_c refers to the accumulative slip when the stress declines to the

Figure 4. Comparison between three-component velocity waveforms of accelerometers and of the nearby broadband stations for (a) Zhaotong and (b) Qiaojia stations. Black lines are the recovered velocity waveforms from the accelerometers, in which −1 is multiplied by the acceleration data for polarity flipping, and the pre-event mean in each acceleration is removed before integral. Red lines show the velocity waveforms from the broadband stations with instrument responses removed. The color version of this figure is available only in the electronic edition.

dynamic friction level (Fig. 1b). According to the proximity of the time moments of stress breakdown and peak slip velocity (Fukuyama *et al.*, 2003; Mikumo *et al.*, 2003), the displacement at peak slip velocity (D_c') could be an approximation of D_c. In reality, it is barely possible to have instruments located exactly on the ruptured fault trace. For the off-fault station, assuming that the displacement is roughly equal on both sides of the strike-slip fault, double of the fault-parallel ground displacement at the time moment of peak fault-parallel ground velocity, namely D_c'', is calculated as a further approximation of the critical slip-weakening distance D_c (Fig. 1c). According to the definition, when dealing with strong-motion data, we need to integrate the original acceleration data properly into velocity and then displacement for obtaining the D_c'' value. Therefore, to recover reliable velocity and displacement is essential for the accurate calculation of D_c''.

Accelerometer performance inspection using nearby broadband station

To calculate the D_c'' value and study the earthquake source process demands the information in velocity and displacement waveforms. At a close distance from the fault, the only available instrument is the accelerometer. To confirm that the displacement and velocity integrated from the accelerograms are reliable, we inspect the velocity waveforms integrated from the same kind of accelerometers in other areas where close broadband stations are also available, so as to compare the waveforms from accelerometers and nearby broadband stations. By exploring the regional broadband stations of China Digital Seismic Observation Network, we find that the regional permanent broadband seismometers are in the proximity of the accelerometers in Zhaotong and Qiaojia, and all recorded

the Ludian earthquake (Fig. 3a). For the strong-motion stations in Zhaotong and Qiaojia, they are equipped with the same instrument as in the LLT station. The interstation distance between the accelerometer and broadband station is around 0.8 km in Zhaotong and is around 2.1 km in Qiaojia, which are both negligible compared to the epicenter distances (ranging from ~44 km to ~46 km). Therefore, we inspect the integrated waveforms of the accelerometers at the two spots using the broadband waveforms as references.

When comparing the velocity waveforms integrated from the accelerometers with those on the adjacent broadband stations, we find that the polarity of the strong-motion data is opposite to that of the broadband station. The waveform comparison is striking at Zhaotong stations, as the accelerometer and broadband station are very close to each other. After flipping the polarity of the velocity data from the accelerometer, the velocity waveforms show high consistency on three components (Fig. 4a). Because of the strong ground shaking induced by the Ludian earthquake, the broadband stations exhibit waveforms clipping at the station over 40 km from the epicenter. Nonetheless, the initial segment after *P*-wave
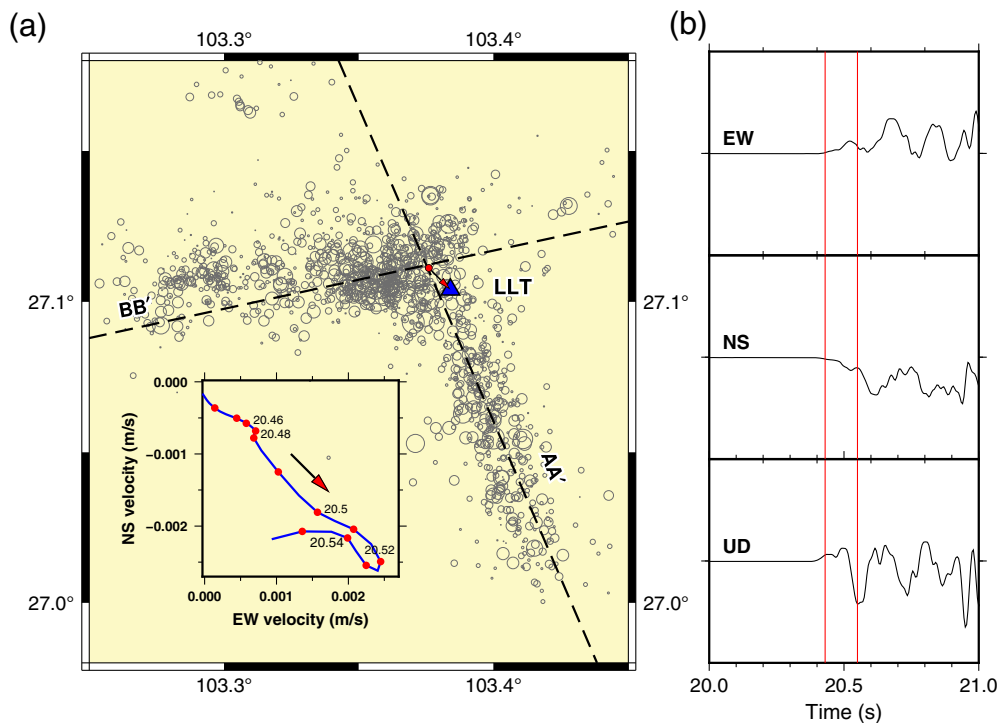
Figure 5. (a) Estimation of the epicenter (the red solid circle at the arrow end) from the particle motion. The blue triangle stands for the LLT station. Hollow circles represent the aftershock distribution. Dashed lines are two inferred fault traces adopted in Niu *et al*. (2020). The subfigure inserted in the map shows the particle motion diagram for horizontal velocities obtained from the LLT station. The red dots appear at 0.01 s intervals, and the numbers indicate the time points from the time series. The red arrows indicate an azimuth = 135°. (b) The three-component velocity waveform segments. The red lines highlight the section used in the particle motion trace in (a). The color version of this figure is available only in the electronic edition.

development process for the Ludian earthquake have been intriguing due to the complex geometry of the conjugate faults and the location uncertainties. Here, given the near-field observation, we integrate the velocity waveforms from the LLT station and visualize the initial stage particle motion (Fig. 5). The *P*-wave arrives at ~20.4 s on the three-component velocity waveforms (Fig. 5b). At the initial stage after the *P* arrival, the horizontal particle motion shows a northwest to southeast movement, and the movement direction is close to 135° (Fig. 5a). Tracing the initial point back according to the movement direction, we find that the direction vector intersects with the fault traces and the aftershock cluster at the crossing part of the two fault branches. Combing the tracing result of the epicenter and the slip patch distribution (Niu *et al.*, 2020), it indicates a rupture initiation from the intersection of the fault branches and propagating toward southeast, causing main slip patches in the southeast portion of the fault. The initiation location at the intersection is consistent with the hypocenters used in the finite-fault inversion studies (Liu *et al.*, 2014; Luo *et al.*, 2018). The southeast direction rupture propagation is also supported by the rupture directivity analyses (Zhao *et al.*, 2014; He *et al.*, 2015). It confirms that the rupture propagates through the fault segment close to the LLT station, and makes the LLT station a great position for applying D_c'' method and probing the earthquake source.

Recovering displacement and calculating D_c'' from accelerogram

D_c'' is essentially near-field displacement in the fault-parallel direction. We first rotate the horizontal accelerograms in north-east coordinate system to the fault-parallel and fault-normal directions. The fault strike direction is set at 337° in accordance with the fault geometry in the previous inversion study constrained by the aftershock distribution (Niu *et al.*, 2020). To obtain the displacement and velocity from the accelerograms requires integral of the acceleration; small errors could be largely magnified after the integral and double

arrival within the scale range of the broadband seismometer is almost identical to that integrated from the accelerometer (Fig. 4a), and the later clipped segment shows accordant phase with the integrated velocity. The slight deviation on the coda part could be caused by the baseline drift of the accelerometer. For the Qiaojia stations, due to the larger interstation distance (~2.1 km) between the accelerometer and the broadband station, the waveform consistency is lower than that in the Zhaotong stations, but we can still observe a good coherence on the long-period trend of the initial segment after shifting the polarity (Fig. 4b). Therefore, we reckon that the polarity of the strong-motion station is in the opposite way of the broadband station tradition. The velocity movement at the LLT station after polarity shifting is consistent with the left-lateral movement feature of the Baogunao–Xiaohe fault.
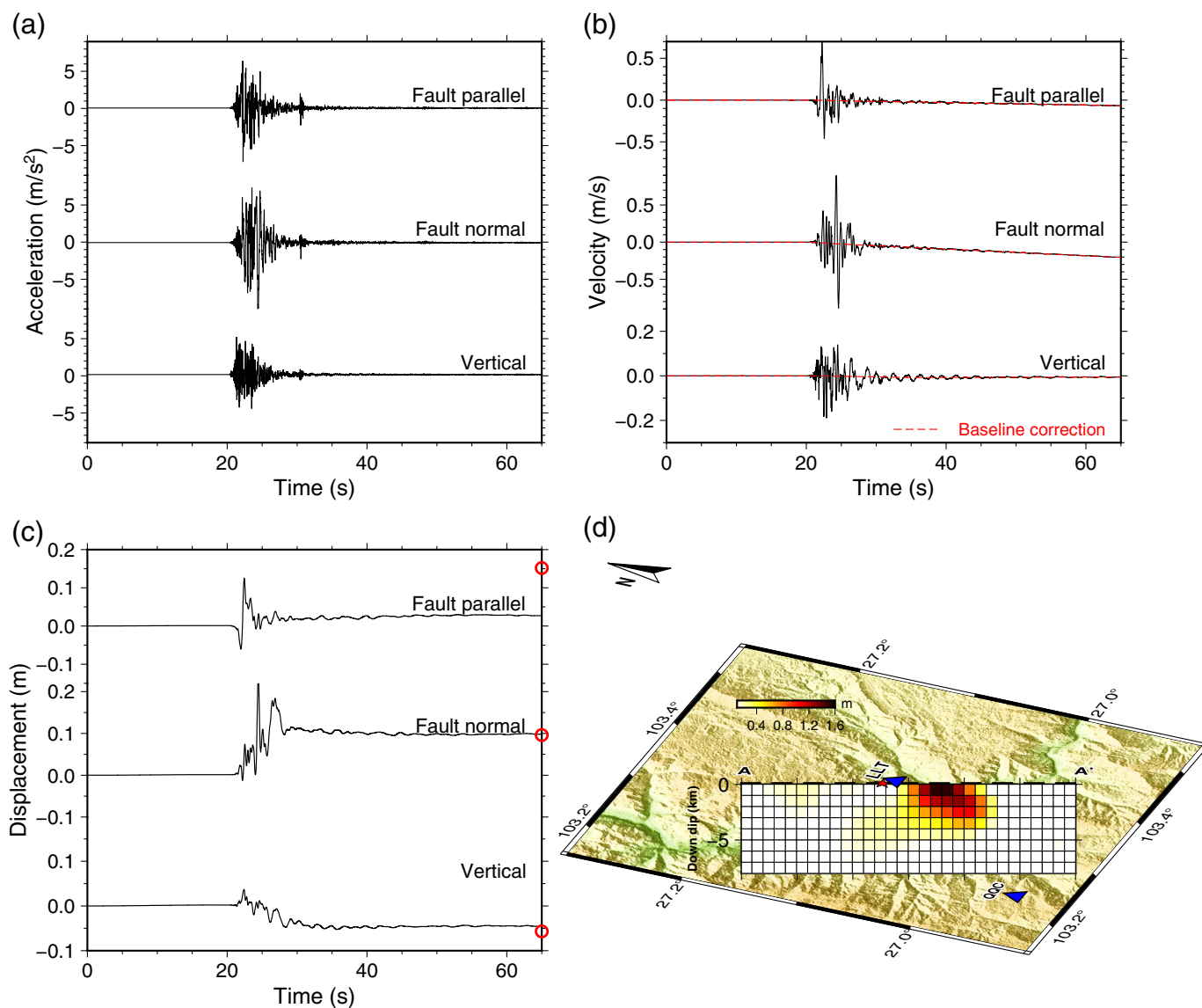
Results
Estimating epicenter from particle motion

To better utilize the D_c'' method for D_c estimation, one of the assumptions is that the earthquake rupture should pass through the fault segment close to the station. The rupture initiation and

Figure 6. (a) Original three-component accelerograms output from the LLT station. Horizontal components are rotated to the fault-parallel and fault-normal directions. (b) Three-component velocity waveforms before the baseline shift correction (black) and linear fitting of the baseline drift (red dashed). (c) Three-component displacement waveforms recovered after the baseline correction in (b). Red circles show the predicted displacements of the finite-fault model from Niu *et al.* (2020). (d) Location of the LLT station and the coseismic slip patches on the fault profile AA′ inverted by Niu *et al.* (2020). The red star shows the estimated epicenter from Figure 5a on the ground. The color version of this figure is available only in the electronic edition.

integral. One of the significant biases comes from the instrument tilting (Graizer, 2005). As the near-fault accelerometer experiences intense ground deformation, it may cause instrument slant and lead to baseline drift, which will produce improper velocity and displacement after integral. To recover reliable velocity and displacement and calculate the D_c'' accurately, we conduct baseline adjustment and correction to the acceleration data (Fig. 6).

In principle, the acceleration value should be zero in the resting period before the disturbance of seismic waves, whereas, in reality, the original acceleration value might be deviated from zero due to noises and initial instrument deviation. For example, the mean acceleration value in the pre-event period is ∼0.064 m/s² in the fault-parallel component (Fig. 6a); such a small amount will lead to the velocity overwhelmed by a strong linear trend with a slope of 0.064 m/s² ending up at a velocity over 4 m/s after the 65 s time history. To remove the pre-event nonzero values,

we calculate the mean value of the initial 18 s for each of the three-component acceleration records and subtract the pre-event mean values from the entire records.

After removing the pre-event acceleration values and conducting integral, velocities are around zero before the arrival of

earthquake waveforms, but the strong linear trends occur on the three components after the passage of earthquake waves, indicating that baseline drift happened on the station (Fig. 6b). The baseline drift is prominent on two horizontal components and is less significant on the vertical component, which could be explained by the less sensitivity of the vertical sensor to tilting (Boore, 2001; Graizer, 2005). The velocities do not return to zero after the subsiding of seismic waves, which is contrary to the common sense and will lead to huge spurious displacements. Therefore, baseline correction should be conducted to remove the linear trends and recover the true velocity waveforms.

We adopt the two-segment linear fitting to fit the trend on each component (Boore, 2001): two linear fitting trends with different slopes in the time segment $t_1 \sim t_2$ and in t_2 to the end are subtracted from the velocity waveform. For the stable linear trend in the end part of the waveform, we use least-squares linear fitting to fit the data between $t_{f1} = 40$ s and $t_{f2} = 64$ s with the fitting equation as follows:

$$v_f(t) = v_0 + a_f t.$$

The coefficients v_0 and a_f are obtained from the linear fitting. We choose t_{f1} and t_{f2} at where the earthquake waves have subsided. The fitting trend is removed from the velocity waveform from t_2 to the end.

For the former segment $t_1 \sim t_2$, a linear baseline correction with slope $= a_m$ is performed on the velocity record, which is a simplification of the complex change in the baseline during the strong ground shaking. The linear trend gradually grows from 0 to connecting with the v_f at t_2, and the a_m is given by

$$a_m = \frac{v_f(t_2)}{t_2 - t_1}.$$

The t_1 and t_2 are free parameters, and the choices of t_1 and t_2 might lead to different final correction results. We test different t_1 values around the starting of strong ground shaking when the acceleration component exceeds 50 cm/s^2 (Iwan et al., 1985; Boore, 2001). For the acceleration of three components, the starting time points for strong ground shaking are between 20 and 21 s. For t_2, we investigate various values between t_1 and t_{f1} to conduct the corrections. After testing, we chose $t_1 = 20.5$ s, $t_2 = 22$ s for the fault-parallel component, $t_1 = 20.9$ s, $t_2 = 23$ s for the fault-normal component, and $t_1 = 22$ s, $t_2 = 35$ s for the vertical component to conduct the two-segment baseline correction.

Using the method mentioned earlier, we correct the baseline shift (Fig. 6b) and integrate the corrected velocities into displacements (Fig. 6c). After the correction, the recovered displacements show near stable permanent displacements at the end of the records. According to the definition of D_c'', at the time point of peak fault-parallel ground velocity, the double
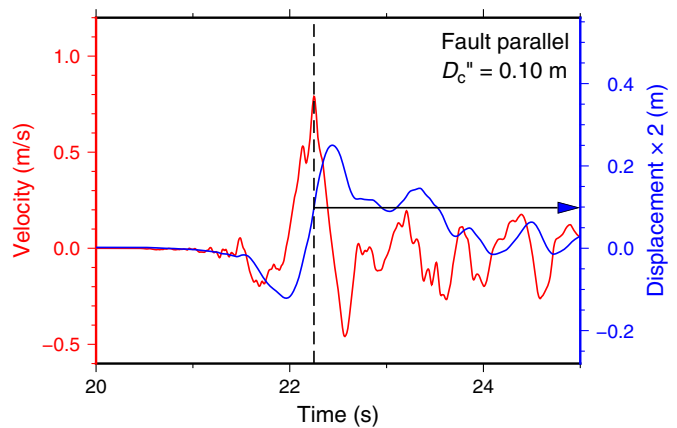
Figure 7. Displacement (blue) and velocity (red) waveforms in the fault-parallel direction from the LLT station. Dashed line marks the time point of the peak fault-parallel velocity; double of the corresponding fault-parallel displacement at the time point, that is, D_c'', is 0.1 m (pointed by the arrow). The color version of this figure is available only in the electronic edition.

cumulative fault-parallel displacement is the D_c'' value. We combine the corrected velocity and displacement in the fault-parallel component and obtain a $D_c'' = 0.1$ m from the records (Fig. 7).

According to Cruz-Atienza et al. (2009), to ensure the D_c'' containing information on the fault weakening requires the station off-fault distance within the resolution distance R_c. They proposed that $R_c \approx 0.8 V_S T_c$, in which V_S refers to the S-wave speed, and the breakdown time T_c could be approximated from the time when the displacement starts to grow until the peak velocity time. V_S is 3.2 km/s according to the explosion seismic profile and the receiver function result (Xiong et al., 1993; Wang et al., 2014). We estimate T_c at around 0.3 s from the waveform (Fig. 7). Substituting the values into the equation, we get $R_c \approx 0.77$ km, and the LLT station falls within the resolution distance. Thus, our D_c'' calculation from the LLT station may provide information on the critical slip-weakening distance D_c.

Discussion
Constraints on the final displacements from inversion results

One of the indicators of the proper baseline correction performance is that the recovered displacement shows stable residual displacement at the end of the record. However, as tested by Boore (2001), correction schemes with various choices of t_1 and t_2 could lead to different plausible final displacements. Appropriate correction parameters and accurate velocity and displacement require additional constraints on the final displacement, such as the Global Positioning System (GPS) measurements and Interferometric Synthetic Aperture Radar (InSAR) observations. However, GPS stations near

the Ludian region are relatively sparse and far from the fault (Wei *et al.*, 2018); for InSAR data, the near-fault region shows low coherence to resolve reliable coseismic displacements (Niu *et al.*, 2020). In this study, we use the fault slip model of Niu *et al.* (2020) that was constrained by InSAR and GPS data to calculate the predicted ground displacements and use the values to serve as additional constraints on the recovered displacements.

We calculate the coseismic ground deformation using the finite element code PyLith (Aagaard *et al.*, 2013). We set a kinematic fault model with prescribed slip amounts and planer fault dip angle as the same as that of the northwest–southeast fault in Niu *et al.* (2020), and output the ground displacements at the station position (Fig. 6d). The predicted ground displacements at the station location are in good agreement with the final displacements on the fault-normal and vertical components, whereas the fault-parallel component is overestimated compared to the final displacement integrated from the accelerogram (Fig. 6c). Given the nature of the strike-slip faulting, we expect a larger displacement in the fault-parallel direction. The fault-parallel component from the strong-motion data might show an undervaluation on the final displacement.

The discrepancy in the fault-parallel direction could be related to the lack of low-frequency components removed by the built-in filter of the accelerograph. According to the calibration work of station PS10 after the 2002 M_w 7.9 Denali earthquake, which is equipped with Honey well Sundstrand Q-Flex accelerometer sensors (Ellsworth *et al.*, 2004), the loss of low-frequency energy could lead to the dramatic underestimation of the permanent displacement. We check the spectrum of the acceleration records on the LLT station and observe a lack of frequency component lower than ∼0.2 Hz (Fig. 8). Details about the low-cut frequency of the processing system are not available from the instrument company, as the ETNA accelerograph is obsolete. When a high-pass filter is applied, the inadequacy in low-frequency components could erase the static displacement from the waveform, which could account for the small permanent displacement on the fault-parallel component.

So far, we do not have the opportunity to conduct the onsite calibration, such as the shake table test, for the instrument to evaluate the low-frequency energy loss; fortunately, the undervaluation of static displacement would not pose significant effects on the D_c'' value. The D_c'' is obtained from the ground displacement at the peak velocity time. Removing the low-frequency components would change little of the peak velocity time point. According to the calibration result of the PS10 station (Ellsworth *et al.*, 2004), the restoration of low-frequency energy would cause a monotonically increasing displacement rather than the undulant behavior, and the main changes occur on the later fluctuation part of the displacement. As the D_c'' is obtained at the initial monotonically increasing segment of the displacement of the LLT station, the influence of increasing
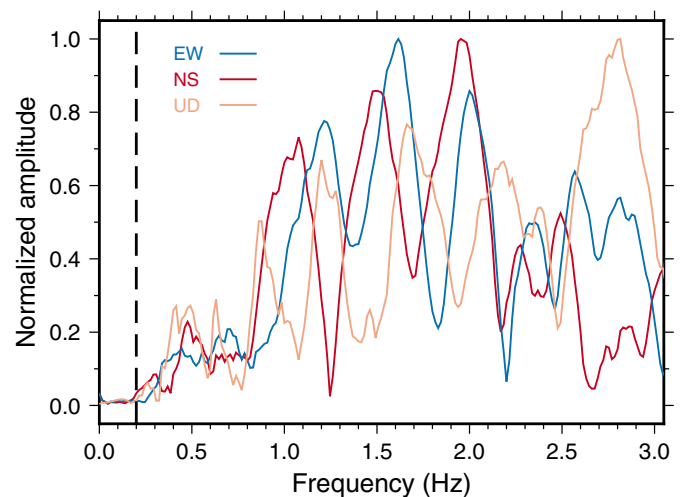
Figure 8. Normalized spectrum for the east–west (blue), north–south (red), and up–down (salmon) components of acceleration at the LLT station. The amplitude is normalized by the maximum value in each component. The black dashed line shows the 0.2 Hz frequency. The pre-event baseline is adjusted for the accelerogram in each component. The color version of this figure is available only in the electronic edition.

final displacement is limited on the D_c'' value. Nevertheless, we could use the total slip value as an upper limit for estimating the critical slip-weakening distance, as D_c is a portion of the total slip. According to the inversion result of Niu *et al.* (2020), the nearest slip patch from the station shows a slip of ∼0.3 m; thus, despite the discrepancy in the final displacements, we could have an estimation value of D_c'' between 0.1 and 0.3 m.

Free-surface effect and potential deviation on D_c'' estimation

The estimation of critical slip-weakening distance from D_c'' is affected by various factors related to the ground velocity and displacement. One important factor is the free-surface amplification, which could impact not only the ground motion but also the rupture features. Cruz-Atienza *et al.* (2009) pointed out that there is no need to double the fault-parallel displacement to account for the displacements in both sides of the fault in the definition of D_c'', as the amplification factor of the free surface is around 2. As such, Cruz-Atienza and Olsen (2010) calculated the D_c'' values for the 1999 İzmit and the 2002 Denali earthquakes after applying the Mach-wave asymptotic correction and near-field adjustment for their supershear ruptures. The estimates of D_c'' were 1.7 m and 1.5 m, respectively, for the two earthquakes. In contrast, Fukuyama and Mikumo (2007) got the estimate of 2.5 m for the 2002 Denali earthquake without taking into account the free-surface effect.

However, the amplification effects of the free surface on D_c'' seem to vary with parameter settings (e.g., fig. 11 in

Cruz-Atienza et al., 2009). In some cases, multiplying a factor 2 or not would lead to similar deviation degrees of D_c'' from the real D_c, which are within the predicted 50% inaccuracy of the method (Fukuyama et al., 2003; Mikumo et al., 2003). Based on other simulation results on D_c'' estimation (Kaneko et al., 2017; Chen and Yang, 2020), the D_c'' values obtained from the doubled fault-parallel displacements show reasonable agreement with the prescribed D_c. Furthermore, there is often a low-velocity zone (LVZ) for crustal faults with widths ranging from hundreds of meters to a few kilometers (e.g., Yang and Zhu, 2010; Yang et al., 2014, 2020; Yang, 2015), which may significantly modulate rupture propagation and slip distribution (Weng et al., 2016). It has been shown that the magnification effects on D_c'' estimation due to the LVZ could exceed 200% compared to the real D_c (Chen and Yang, 2020); thus, it would become a more dominant factor when a prominent LVZ exists in the near-fault area.

Nevertheless, the factor 2 effect due to the free surface might make a significant difference for larger D_c'' estimation values, such as the D_c'' of the 2016 Kaikōura earthquake (4.9 m). In contrast, the impact is quite minor for a small estimation value, such as for the 2014 Ludian earthquake (0.1 m). So in this study, we follow the definition of Fukuyama and Mikumo (2007) and calculate D_c'' from the doubled fault-parallel displacement.

Apparent scaling of D_c''

Among all the earthquakes with D_c'' calculation, the 2014 Ludian earthquake is the smallest earthquake so far. We added the D_c'' value of the Ludian earthquake into the comparison between D_c'' and the fault slip, together with the previous five earthquakes (Fig. 9). We derive a new scaling relationship with the least-squares fitting of the six events, in which the Denali earthquake was taken the average of the two estimates from different approaches (Fukuyama and Mikumo, 2007; Cruz-Atienza and Olsen, 2010). We find that the obtained fitting relationship does not change much compared to that in Kaneko et al. (2017), who did not include the D_c'' values for the Ludian earthquake, the İzmit earthquake, and the Denali estimation with the Mach-wave asymptotic correction. The D_c'' value of the Ludian earthquake follows the scaling relationship of D_c'' and the fault slip for the previous larger earthquakes (Fig. 9). Comparing to the final slip on the nearest fault grid from the inversion model (Niu et al., 2020), the D_c'' value accounts for around 33% of the final slip (Table 1).

However, this may not necessarily indicate that the critical slip-weakening distance D_c takes a roughly constant percentage of the total slip. Because D_c'' is essentially the near-field displacement, which is directly affected by the magnitude of the earthquake, the increase of D_c'' with fault slip is an apparent scaling, rather than a representation of the scaling of real D_c on the fault (Chen and Yang, 2020). Besides, in dynamic
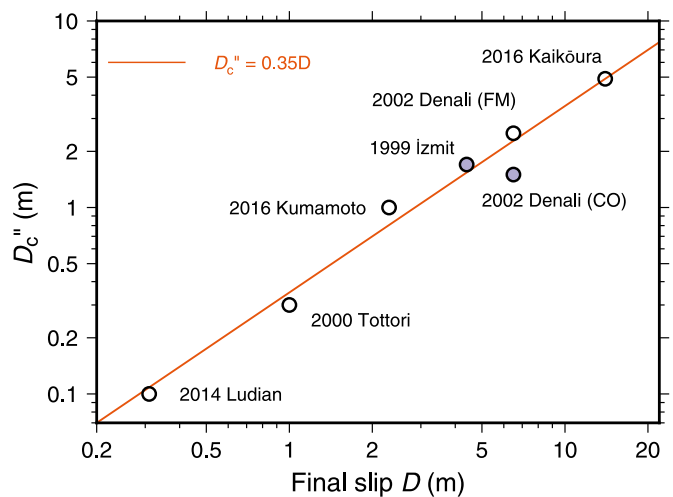
Figure 9. Comparison between the D_c'' values and the corresponding final slip D. The two purple dots indicate the two D_c'' estimates with the Mach-wave asymptotic correction and near-field adjustment applied (Cruz-Atienza and Olsen, 2010). The orange line shows the least-squares fitting of the data points. The color version of this figure is available only in the electronic edition.

rupture simulations comparing with near-field observations (Weng and Yang, 2018; Yao and Yang, 2020), synthetic near-field ground velocities show no distinct differences in models with heterogenous slip-scaled D_c and a constant prescribed D_c. To distinguish the scale dependency of D_c is challenging and demands further work to investigate.

Conclusion

In this study, we conduct waveform analyses of the near-fault accelerometer data associated with the 2014 Ludian earthquake. We estimate the initiation of the rupture from the particle motion analysis and validate that the earthquake rupture passed through the accelerometer. We conduct baseline correction for the accelerometer data with pre-event adjustment and velocity drift fitting, and recover the ground velocities and displacements from the accelerograms. We calculate the predicted ground displacements of a kinematic fault model as additional constraints on the displacements and the baseline correction scheme. Using the data of the near-fault strong-motion station, we obtain an estimation value $D_c'' = 0.1$ m for the critical slip-weakening distance by combining the recovered velocity and displacement in the fault-parallel direction. As the smallest event with the D_c'' value, the Ludian earthquake follows the apparent scaling law of the D_c'' with fault slip. This work presents a workflow for processing near-fault accelerometer data to recover near-field velocities and displacements. The obtained D_c'' value provides a reference value of the critical slip-weakening distance for the 2014 M_w 6.2 Ludian earthquake and could be incorporated into future numerical studies.

Data and Resources

The seismograms in this study are provided by the Yunnan Earthquake Agency. The regional earthquake catalog is obtained from National Earthquake Data Center (https://data.earthquake.cn). We searched the Global Centroid Moment Tensor (Global CMT) database for earthquake focal mechanisms (https://www.globalcmt.org, Dziewonski et al., 1981; Ekström et al., 2012). Seismic Analysis Code (SAC), ObsPy 1.2.1 (doi: 10.5281/zenodo.3706479), SciPy (Virtanen et al., 2020), and NumPy (Harris et al., 2020) are used for data analysis. The figures are made using Generic Mapping Tools (GMT, Wessel and Smith, 1998). All websites were last accessed in November 2020.

Declaration of Competing Interests

The authors acknowledge that there are no conflicts of interest recorded.

Acknowledgments

References

Aagaard, B. T., M. G. Knepley, and C. A. Williams (2013). A domain decomposition approach to implementing fault slip in finite-element models of quasi-static and dynamic crustal deformation, *J. Geophys. Res.* **118,** no. 6, 3059–3079, doi: 10.1002/jgrb.50217.

Andrews, D. J. (1976a). Rupture propagation with finite stress in antiplane strain, *J. Geophys. Res.* **81,** no. 20, 3575–3582, doi: 10.1029/JB081i020p03575.

Andrews, D. J. (1976b). Rupture velocity of plane strain shear cracks, *J. Geophys. Res.* **81,** no. 32, 5679–5687, doi: 10.1029/JB081i032p05679.

Boore, D. M. (2001). Effect of baseline corrections on displacements and response spectra for several recordings of the 1999 Chi-Chi, Taiwan, earthquake, *Bull. Seismol. Soc. Am.* **91,** no. 5, 1199–1211, doi: 10.1785/0120000703.

Chen, X., and H. Yang (2020). Effects of seismogenic width and low-velocity zones on estimating slip-weakening distance from near-fault ground deformation, *Geophys. J. Int.* **223,** no. 3, 1497–1510, doi: 10.1093/gji/ggaa385.

Cheng, J., Z. Wu, J. Liu, C. Jiang, X. Xu, L. Fang, X. Zhao, W. Feng, R. Liu, J. Liang, et al. (2015). Preliminary report on the 3 August 2014, Mw 6.2/Ms 6.5 Ludian, Yunnan-Sichuan Border, Southwest China, earthquake, *Seismol. Res. Lett.* **86,** no. 3, 750–763, doi: 10.1785/0220140208.

Cruz-Atienza, V. M., and K. B. Olsen (2010). Supershear Mach-waves expose the fault breakdown slip, *Tectonophysics* **493,** nos. 3/4, 285–296, doi: 10.1016/j.tecto.2010.05.012.

Cruz-Atienza, V. M., K. B. Olsen, and L. A. Dalguer (2009). Estimation of the breakdown slip from strong-motion seismograms: Insights from numerical experiments, *Bull. Seismol. Soc. Am.* **99,** no. 6, 3454–3469, doi: 10.1785/0120080330.

Dziewonski, A. M., T. A. Chou, and J. H. Woodhouse (1981). Determination of earthquake source parameters from waveform data for studies of global and regional seismicity, *J. Geophys. Res.* **86,** no. B4, 2825–2852, doi: 10.1029/JB086iB04p02825.

Ekström, G., M. Nettles, and A. M. Dziewoński (2012). The global CMT project 2004–2010: Centroid-moment tensors for 13,017 earthquakes, *Phys. Earth Planet. In.* **200/201,** 1–9, doi: 10.1016/j.pepi.2012.04.002.

Ellsworth, W. L., M. Celebi, J. R. Evans, E. G. Jensen, R. Kayen, M. C. Metz, D. J. Nyman, J. W. Roddick, P. Spudich, and C. D. Stephens (2004). Near-field ground motion of the 2002 Denali fault, Alaska, earthquake recorded at pump station 10, *Earthq. Spectra* **20,** no. 3, 597–615, doi: 10.1193/1.1778172.

Fang, L. H., J. P. Wu, W. L. Wang, Z. Y. Lv, C. Z. Wang, T. Yang, and S. J. Zhong (2014). Relocation of the aftershock sequence of the Ms 6.5 Ludian earthquake and its seismogenic structure, *Seismol. Geol.* **36,** no. 4, 1173–1185 (in Chinese).

Fukuyama, E., and T. Mikumo (2007). Slip-weakening distance estimated at near-fault stations, *Geophys. Res. Lett.* **34,** no. 9, 2–6, doi: 10.1029/2006GL029203.

Fukuyama, E., and W. Suzuki (2016). Near-fault deformation and Dc″ during the 2016 Mw7.1 Kumamoto earthquake, *Earth Planets Space* **68,** no. 1, 6–11, doi: 10.1186/s40623-016-0570-6.

Fukuyama, E., T. Mikumo, and K. B. Olsen (2003). Estimation of the critical slip-weakening distance: Theoretical background, *Bull. Seismol. Soc. Am.* **93,** no. 4, 1835–1840, doi: 10.1785/0120020184.

Goto, H., and S. Sawada (2010). Trade-offs among dynamic parameters inferred from results of dynamic source inversion, *Bull. Seismol. Soc. Am.* **100,** no. 3, 910–922, doi: 10.1785/0120080250.

Graizer, V. M. (2005). Effect of tilt on strong motion data processing, *Soil Dynam. Earthq. Eng.* **25,** no. 3, 197–204, doi: 10.1016/j.soildyn.2004.10.008.

Guatteri, M., and P. Spudich (2000). What can strong-motion data tell us about slip-weakening fault-friction laws? *Bull. Seismol. Soc. Am.* **90,** no. 1, 98–116, doi: 10.1785/0119990053.

Harris, C. R., K. J. Millman, S. J. van der Walt, R. Gommers, P. Virtanen, D. Cournapeau, E. Wieser, J. Taylor, S. Berg, N. J. Smith, et al. (2020). Array programming with NumPy, *Nature* **585,** no. 7825, 357–362, doi: 10.1038/s41586-020-2649-2.

He, X. H., S. D. Ni, and J. Liu (2015). Rupture directivity of the August 3rd, 2014 Ludian earthquake (Yunan, China), *Sci. China Earth Sci.* **58,** no. 5, 795–804, doi: 10.1007/s11430-015-5053-2.

Ida, Y. (1972). Cohesive force across the tip of a longitudinal-shear crack and Griffith's specific surface energy, *J. Geophys. Res.* **77,** no. 20, 3796–3805, doi: 10.1029/JB077i020p03796.

Iwan, W. D., M. A. Moser, and C. Peng (1985). Some observations on strong-motion earthquake measurement using a digital accelerograph, *Bull. Seismol. Soc. Am.* **75,** no. 5, 1225–1246.

Jiang, X., H. Yang, W. Yang, and W. Wang (2020). Crustal structure in the Binchuan Basin of Yunnan constrained from receiver functions on a 2-D seismic dense array, *Earthq. Sci.* **33,** 264–272, doi: 10.29382/eqs-2020-0264-01.

Kaneko, Y., E. Fukuyama, and I. J. Hamling (2017). Slip-weakening distance and energy budget inferred from near-fault ground deformation during the 2016 Mw7.8 Kaikōura earthquake, *Geophys. Res. Lett.* **44,** no. 10, 4765–4773, doi: 10.1002/2017GL073681.

Li, X., X. Xu, Y. Ran, J. Cui, Y. Xie, and F. Xu (2015). Compound fault rupture in the 2014 Ms 6.5 Ludian, China, earthquake and significance to disaster mitigation, *Seismol. Res. Lett.* **86,** no. 3, 764–774, doi: 10.1785/0220140198.

Liu, C., Y. Zheng, X. Xiong, R. Fu, B. Shan, and F. Diao (2014). Rupture process of Ms6.5 Ludian earthquake constrained by regional broadband seismograms, *Chin. J. Geophys.* **57,** no. 9, 3028–3037, doi: 10.6038/cjg20140927 (in Chinese).

Luo, Y., M. C. Hsieh, and L. Zhao (2018). Source rupture process of the 2014 Ms 6.5 Ludian, Yunnan, China, earthquake in 3D structure: The strain green's tensor database approach, *Bull. Seismol. Soc. Am.* **108,** no. 6, 3270–3277, doi: 10.1785/0120180090.

Mikumo, T., K. B. Olsen, E. Fukuyama, and Y. Yagi (2003). Stress-breakdown time and slip-weakening distance inferred from slip-velocity functions on earthquake faults, *Bull. Seismol. Soc. Am.* **93,** no. 1, 264–282, doi: 10.1785/0120020082.

Niu, Y., S. Wang, W. Zhu, Q. Zhang, Z. Lu, C. Zhao, and W. Qu (2020). The 2014 Mw 6.1 Ludian earthquake: The application of RADARSAT-2 SAR interferometry and GPS for this conjugated ruptured event, *Remote Sens.* **12,** no. 1, 99, doi: 10.3390/rs12010099.

Virtanen, P., R. Gommers, T. E. Oliphant, M. Haberland, T. Reddy, D. Cournapeau, E. Burovski, P. Peterson, W. Weckesser, J. Bright, *et al.* (2020). SciPy 1.0: Fundamental algorithms for scientific computing in Python, *Nat. Methods* **17,** no. 3, 261–272, doi: 10.1038/s41592-019-0686-2.

Wang, W. L., J. P. Wu, L. H. Fang, and G. J. Lai (2014). Double difference location of the Ludian *Ms* 6.5 earthquake sequences in Yunnan province in 2014, *Chin. J. Geophys.* **57,** no. 9, 3042–3051, doi: 10.6038/cjg20140929 (in Chinese).

Wei, W. X., Z. S. Jiang, D. S. Shao, Z. G. Shao, X. X. Liu, Z. Y. Zou, and Y. Wang (2018). Coseismic displacements from GPS and inversion analysis for the 2014 Ludian 6.5 earthquake, *Chin. J. Geophys.* **61,** no. 4, 1258–1265, doi: 10.6038/cjg2018L0141 (in Chinese).

Weng, H., and H. Yang (2018). Constraining frictional properties on fault by dynamic rupture simulations and near-field observations, *J. Geophys. Res.* **123,** no. 8, 6658–6670, doi: 10.1029/2017JB015414.

Weng, H., H. Yang, Z. Zhang, and X. Chen (2016). Earthquake rupture extents and coseismic slips promoted by damaged fault zones, *J. Geophys. Res.* **121,** no. 6, 4446–4457, doi: 10.1002/2015JB012713.

Wessel, P., and W. H. F. Smith (1998). New, improved version of generic mapping tools released, *Eos Trans. AGU* **79,** no. 47, 579–579, doi: 10.1029/98eo00426.

Xiong, S., Y. Zheng, Z. Yin, X. Zeng, Y. Quan, and K. Sun (1993). The 2-D structure and its tectonic implications of the crust in the Lijiang-Panzhihua-Zhehuai region, *Acta Geophys. Sin.* **36,** no. 4, 434–444 (in Chinese).

Xu, X., C. Xu, G. Yu, X. Wu, X. Li, and J. Zhang (2015). Primary surface ruptures of the Ludian Mw 6.2 earthquake, southeastern Tibetan Plateau, China, *Seismol. Res. Lett.* **86,** no. 6, 1622–1635, doi: 10.1785/0220150038.

Yang, H. (2015). Recent advances in imaging crustal fault zones: A review, *Earthq. Sci.* **28,** no. 2, 151–162, doi: 10.1007/s11589-015-0114-3.

Yang, H., and S. Yao (2021). Shallow destructive earthquakes, *Earthq. Sci.* **34,** doi: 10.29382/eqs-2020-0072.

Yang, H., and L. Zhu (2010). Shallow low-velocity zone of the San Jacinto fault from local earthquake waveform modeling, *Geophys. J. Int.* **183,** no. 1, 421–432, doi: 10.1111/j.1365-246X.2010.04744.x.

Yang, H., Y. Duan, J. Song, X. Jiang, X. Tian, W. Yang, W. Wang, and J. Yang (2020). Fine structure of the Chenghai fault zone, Yunnan, China, constrained from teleseismic travel time and ambient noise tomography, *J. Geophys. Res.* **125,** no. 7, 1–14, doi: 10.1029/2020JB019565.

Yang, H., Y. Duan, J. Song, W. Yang, W. Wang, X. Tian, and B. Wang (2021). Illuminating high-resolution crustal fault zones and temporal changes using multi-scale dense arrays and airgun sources, *Earthq. Res. Adv.* **1,** no. 1, doi: 10.1016/j.eqrea.2021.100001.

Yang, H., Z. Li, Z. Peng, Y. Ben-Zion, and F. Vernon (2014). Low-velocity zones along the San Jacinto Fault, Southern California, from body waves recorded in dense linear arrays, *J. Geophys. Res.* **119,** no. 12, 8976–8990, doi: 10.1002/2014JB011548.

Yao, S., and H. Yang (2020). Rupture dynamics of the 2012 Nicoya Mw 7.6 earthquake: Evidence for low strength on the megathrust, *Geophys. Res. Lett.* **47,** no. 13, 1–11, doi: 10.1029/2020GL087508.

Zhang, G. W., J. S. Lei, S. S. Liang, and C. Q. Sun (2014). Relocations and focal mechanism solutions of the 3 August 2014 Ludian, Yunnan Ms6.5 earthquake sequence, *Chin. J. Geophys.* **57,** no. 9, 3018–3027, doi: 10.6038/cjg20140926 (in Chinese).

Zhang, Y., L. S. Xu, Y. T. Chen, and R. F. Liu (2014). Rupture process of the 3 August 2014 Ludian, Yunnan, Mw6.1 (Ms6.5) earthquake, *Chin. J. Geophys.* **57,** no. 9, 3052–3059, doi: 10.6038/cjg20140930 (in Chinese).

Zhao, X., J. Liu, and W. Feng (2014). The kinematic characteristics of the Ms 6.5 Ludian Yunnan earthquake in 2014, *Seismol. Geol.* **36,** no. 4, 1157–1172 (in Chinese).